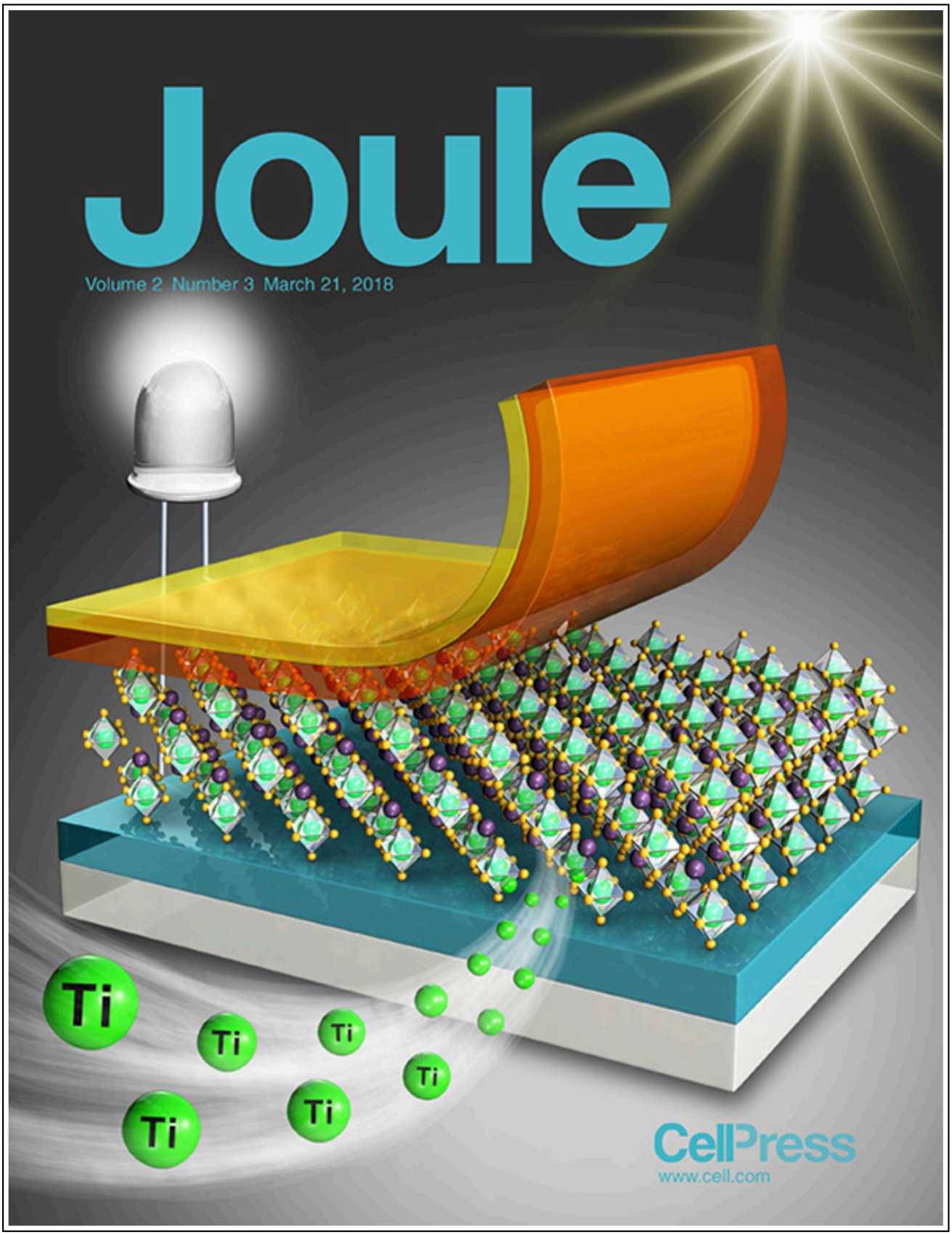

21 March 2018
Volume 2, Issue 3

On the Cover: The prevailing perovskite solar cells employ Pb-based organic-inorganic halide perovskites as light absorbers, raising concerns regarding their inevitable toxicity and instability. In this issue of *Joule*, Chen, Zhou, Padture, et al. (pp. 558–570) utilize the nontoxic and earth-abundant element Ti to replace Pb in making planar-heterojunction solar cells with Cs_2TiBr_6 perovskite. In the cover image, the green Ti atoms flow into the crystal structures to replace toxic Pb atoms, creating vacancy-ordered double perovskites. Such solar cells show stable efficiency and high open-circuit voltage (>1 V), which can be used to generate electricity from sunlight. Cover art by MyScimage.

Joule

CellPress

Article

Cesium Titanium(IV) Bromide Thin Films Based Stable Lead-free Perovskite Solar Cells

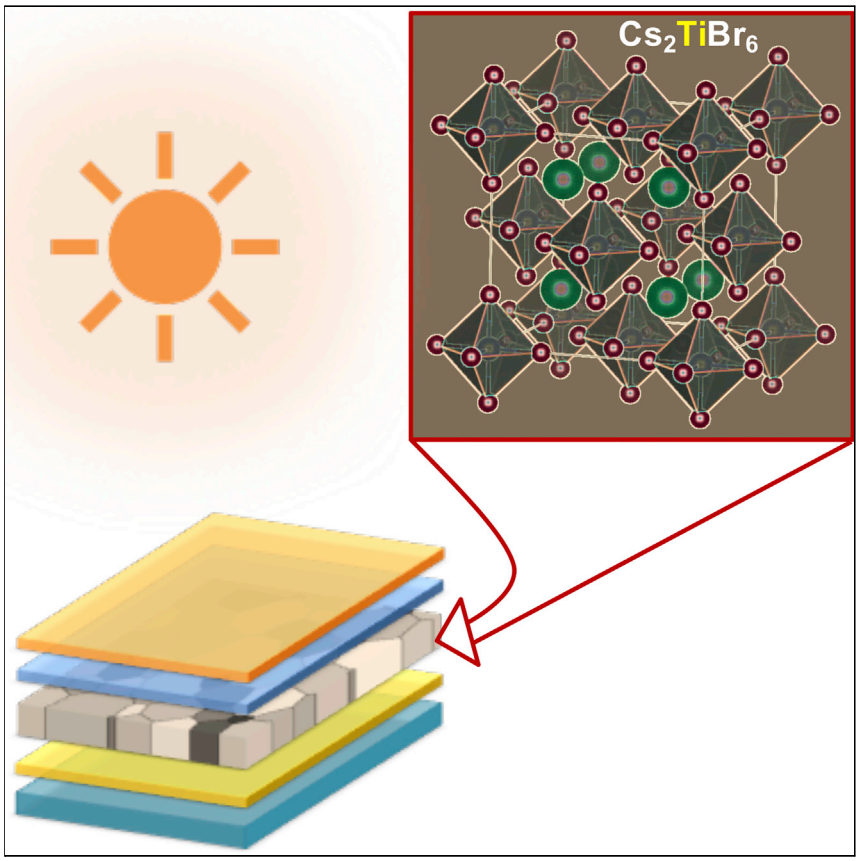

Cesium titanium(IV) halide perovskites (HPs) are promising all-inorganic, Pb-free materials for perovskite solar cells (PSCs). Here we show that high-quality, uniform thin films of Cs_2TiBr_6 HP can be prepared through a facile low-temperature vapor-based method. These thin films exhibit a favorable bandgap of ~1.8 eV, long and balanced carrier-diffusion lengths >100 nm, suitable energy levels, and superior intrinsic and environmental stability. The first planar-heterojunction PSCs based on Cs_2TiBr_6 thin films show a stable efficiency of up to 3.3%.

Min Chen, Ming-Gang Ju, Alexander D. Carl, ..., Xiao Cheng Zeng, Yuanyuan Zhou, Nitin P. Padture

yuanyuan_zhou@brown.edu (Y.Z.)
nitin_padture@brown.edu (N.P.P.)

HIGHLIGHTS

Fabrication of Cs_2TiBr_6 halide perovskite thin films is demonstrated for the first time

Cs_2TiBr_6 thin films have ~1.8 eV bandgap and balanced carrier-diffusion lengths >100 nm

Cs_2TiBr_6 thin films are highly stable under environmental (humidity/heat/light) stresses

First ever solar cells using Cs_2TiBr_6 thin films show a stable efficiency of up to 3.3

Chen et al., Joule 2, 558–570
March 21, 2018
https://doi.org/10.1016/j.joule.2018.01.009

Joule

CellPress

Article

Cesium Titanium(IV) Bromide Thin Films Based Stable Lead-free Perovskite Solar Cells

Min Chen,[1] Ming-Gang Ju,[2] Alexander D. Carl,[3] Yingxia Zong,[1] Ronald L. Grimm,[3] Jiajun Gu,[4] Xiao Cheng Zeng,[2] Yuanyuan Zhou,[1,*] and Nitin P. Padture[1,5,*]

SUMMARY

Significant effort is being devoted to the search for all-inorganic Pb-free halide perovskites (HPs) for photovoltaic applications. However, candidate HPs that combine all the desirable attributes — ease of synthesis, favorable bandgaps, outstanding optoelectronic properties, high stability, no toxicity — are extremely rare. Here, we demonstrate experimentally the promise of cesium titanium(IV) bromide (Cs_2TiBr_6), a part of the Ti-based vacancy-ordered double-perovskite halides family, in perovskite solar cells (PSCs). We show, for the first time, that high-quality Cs_2TiBr_6 thin films can be prepared through a facile low-temperature vapor-based method. These films exhibit a favorable bandgap of ~1.8 eV, long and balanced carrier-diffusion lengths exceeding 100 nm, suitable energy levels, and superior intrinsic and environmental stability. The first demonstration of Cs_2TiBr_6 thin films-based PSCs shows stable efficiency of up to 3.3%. Insights into the Cs_2TiBr_6 film-formation mechanisms and the PSC device operation are provided, pointing to directions for improving Ti-based PSCs.

INTRODUCTION

The rapid emergence of perovskite solar cells (PSCs) as a viable new thin film photovoltaic (PV) technology for single-junction and tandem PV applications has been remarkable.[1–6] The unprecedented combination of high power conversion efficiency (PCE) and potential low cost has been driving the intense PSC research endeavors worldwide. Typical PSCs employ organic-inorganic halide perovskites (OIHPs), such as $CH_3NH_3PbI_3$ ($MAPbI_3$) and $HC(NH_2)_2PbI_3$ ($FAPbI_3$), as light absorbers because they possess an extraordinary combination of desirable optoelectronic properties.[2,5,7,8] However, the volatile organic cations (MA^+, FA^+) and the lead (Pb^{2+}) that are ubiquitous in the state-of-the-art OIHPs are, respectively, responsible for the potential instability and toxicity issues in OIHPs.[9–12] Thus, there is a pressing need to address these major hurdles in the path of commercial deployment of PSCs. Searching for alternative all-inorganic perovskites that are Pb-free and non-toxic is a promising research direction.[13] While several promising candidate materials have been identified, primarily via theoretically predictions, only a few among them have been synthesized successfully. In this context, Sn(II)-based inorganic halide perovskites (HPs) have been the most widely studied.[14–16] In particular, $CsSnI_3$ HP is popular as it possesses a near-ideal bandgap of 1.3 eV suitable for single-junction solar cells. However, the state-of-the-art solar cells based on $CsSnI_3$ HP exhibit very low open circuit voltage (V_{OC}) owing to its intrinsic metallic conductivity.[16] $CsSnI_3$ HP is also found to degrade rapidly under ambient conditions due to the

Context & Scale

Halide perovskites (HPs) have attracted a great deal of attention in the field of photovoltaics (PVs) in recent years. The efficiency of perovskite solar cells (PSCs) has seen an unprecedentedly rapid rise within a short period of time. However, the toxicity of Pb and the volatility of the organic ions in the state-of-the-art HP light absorbers have been recognized as the two major obstacles in the path of PSC development and commercialization. Thus, the search is on for all-inorganic, Pb-free HPs for use in PSCs. In this study, we demonstrate experimentally the promise of a new candidate HP: cesium titanium(IV) bromide, a member of a larger family of Ti-based HPs that are all-inorganic, non-toxic, and contain only earth-abundant elements. The exploration of PSCs based on this new family of HPs is likely to have a lasting impact on the global landscape of environmentally friendly PVs, and these materials may also find use in other promising (opto) electronic applications.

low stability of the crystal structure and the facile oxidation of Sn(II). Furthermore, there could be a certain level of toxicity in Sn-based HPs, as claimed by Babayigit et al.[17] Other promising candidate HPs that have been experimentally synthesized are those based on monovalent and/or trivalent metal cations, such as Ag^{+}, Sb^{3+}, and Bi^{3+}. However, these HPs generally exhibit bandgaps larger than 2.0 eV (e.g. $Cs_3Bi_2I_9$ 2.2 eV, $Cs_2AgBiBr_6$ 2.2 eV, and $Cs_3Sb_2I_9$ 2.4 eV),[18–20] making them unsuitable for most PV applications. In a parallel study, we report the theoretical prediction and experimental synthesis (powders) of a new family of HPs based on Ti(IV), namely Cs_2TiX_6 (X = I or/and Br), with tunable bandgaps.[21] Since Cs_2TiX_6 exhibits a vacancy-ordered double-perovskite structure, where Ti is in its stable +4 oxidation state, Cs_2TiX_6 is expected to possess very high tolerance to the environmental stresses. Ti is also earth-abundant, non-toxic, and biocompatible. These clear advantages of the Cs_2TiX_6 HPs make these hitherto unexplored materials very promising for use in PSCs.

Herein we report, for the first time, the thin film deposition of a representative Ti-based HP, Cs_2TiBr_6, and provide insights into the film-formation mechanism. Optoelectronic properties of the as-deposited Cs_2TiBr_6 HP thin films are measured, showing an optical bandgap of ~1.8 eV, making them highly suitable for tandem PV applications,[4,6] and balanced electron/hole diffusion lengths exceeding 100 nm. The Cs_2TiBr_6 HP thin films are incorporated into planar-heterojunction PSCs, which show PCE of up to 3.3%. Furthermore, the Cs_2TiBr_6 HP thin films and the first ever Ti-based PSCs show high tolerance to environmental stresses.

RESULTS AND DISCUSSION

Diffusion-Based Mechanism Controls the Cs_2TiBr_6 Perovskite Film Formation

Figure 1A illustrates schematically the vapor-based method that is used for the deposition of Cs_2TiBr_6 HP thin films. Here, a uniform thin film of CsBr is first deposited via thermal evaporation on the substrate. This is followed by annealing the CsBr thin film in a $TiBr_4$-vapor atmosphere at 200°C. The hot $TiBr_4$ vapor is expected to interact with the as-deposited CsBr, forming a uniform Cs_2TiBr_6 thin film:

$$2CsBr(s) + TiBr_4(g) \rightarrow Cs_2TiBr_6(s). \text{ Reaction 1}$$

Since the boiling point of $TiBr_4$ is very low (~230°C), the $TiBr_4$ vapor can be produced by simply heating solid $TiBr_4$ at ambient pressure. The experimental setup for performing this reaction was fabricated in-house, and is shown schematically in Figure S1. The thin film before annealing, after 12-hr annealing, and after 24-hr annealing in $TiBr_4$ vapor are denoted as film I, II, and III, respectively. Figures 1B and 1C show indexed X-ray diffraction (XRD) patterns of the three thin films and their corresponding UV-vis spectra. As seen in Figure 1B, film I contains phase-pure CsBr of high crystallinity. In film II, the intensity of XRD peaks for the CsBr phase is significantly reduced, and the XRD peaks associated with the Cs_2TiBr_6 HP evolve, which confirms the progression of Reaction 1 during the annealing step. The conversion reaction is complete after 24-hr annealing, and only phase-pure Cs_2TiBr_6 HP is found in film III. The X-ray photoelectron spectroscopy (XPS) spectrum for Ti 2*p* in film III is presented in Figure S2, which confirms the +4 oxidation state of Ti. The absence of significant features ascribed to lower oxidation states in Ti in the XPS spectrum indicates that there are no side reactions (e.g., decomposition of $TiBr_4$ into Ti metal and Br_2, etc.). In Figure 1C, while the expected absorption features of CsBr and Cs_2TiBr_6 in film I and film III are respectively shown, film II has the typical mixed absorption feature of the CsBr and Cs_2TiBr_6 phases, which is consistent with the XRD results.

[1]School of Engineering, Brown University, Providence, RI 02912, USA

[2]Department of Chemistry, University of Nebraska - Lincoln, Lincoln, NE 68588, USA

[3]Department of Chemistry and Biochemistry, Worcester Polytechnic Institute, Worcester, MA 01609, USA

[4]State Key Laboratory of Metal Matrix Composites, Shanghai Jiao Tong University, Shanghai 200240, China

[5]Lead Contact

*Correspondence: yuanyuan_zhou@brown.edu (Y.Z.), nitin_padture@brown.edu (N.P.P.)

https://doi.org/10.1016/j.joule.2018.01.009

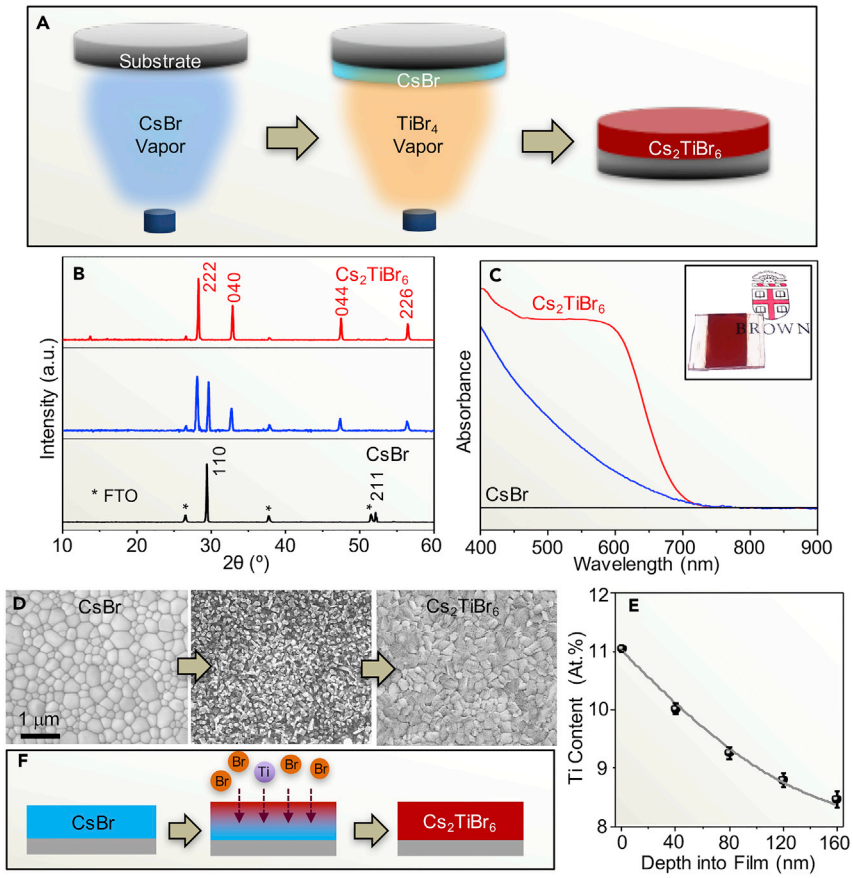

Figure 1. Cs_2TiBr_6 Thin Films Deposition and Its Mechanisms

(A–D) Schematic illustration (A) of the vapor-based synthesis of Cs_2TiBr_6 HP thin film. Vapor-deposited CsBr thin film before annealing (film I), after 12-hr annealing (film II), and after 24-hr annealing (film III) at 200°C. (B) XRD patterns and (C) UV-vis spectra (inset: photograph of the final Cs_2TiBr_6 thin film). The XRD pattern of film III is compared with that of Cs_2TiBr_6 bulk powder in Figure S3. (D) The corresponding SEM images of the surface morphologies of the thin films. See Figure S4 for a cross-sectional SEM image of film III.

(E) Ti content as a function of depth in the intermediate thin film after 12-hr annealing at 200°C (film II).

(F) Proposed mechanism of the formation of the Cs_2TiBr_6 HP thin film.

The inset in Figure 1C is a photograph of the final Cs_2TiBr_6 HP thin film showing an even, dark reddish-brown color and good transparency, confirming its uniformity.

To gain further insights into Reaction 1, we have studied the microstructural and compositional evolution of the thin film as the reaction progresses. Figure 1D shows scanning electron microscopy (SEM) images of the surface morphologies of film I, film II, and film III. Film I is polycrystalline, compact, and pinhole-free, showing a typical microstructure comprising crystalline equiaxed grains and grain boundaries. After 12-hr annealing, the initial smooth film surface becomes relatively rough over the entire film, which implies the uniform occurrence of Reaction 1 with nucleation of Cs_2TiBr_6 HP in the parent CsBr thin film at the surface. Upon the completion of Reaction 1 (24 hr), since there is no more interaction of the solid thin film with $TiBr_4$ vapor, the surface morphology of the thin film is completely reconstructed, which may be due to the thermally induced coarsening of Cs_2TiBr_6 grains, along with the progression of Reaction 1. Thus, film III exhibits uniform grains of Cs_2TiBr_6

HP with well-defined grain boundaries. The Ti content in the intermediate film II was measured as a function of depth. Here, the film II sample (film thickness ~200 nm) was etched locally using focused ion beam (FIB) for different durations, and the Ti content was measured using energy dispersive spectroscopy (EDS) at each depth. Figure 1E shows that the Ti content decreases with depth into film II, which indicates that the reaction progression is driven by the concentration gradient of Ti^{4+} in the thin film. The curve in Figure 1E is a Gauss error-function fit using Fick's second law,[22] which is consistent with thermally activated non-steady-state diffusion of Ti^{4+} in the solid state. The Ti elemental EDS maps at the top surface and surface at 40-nm depth of film II presented in Figure S5 are highly homogeneous, indicating the uniform progression of the diffusion front into the thin film during the $TiBr_4$-vapor-annealing step. Figure S6 plots the Ti content as a function of depth in the final Cs_2TiBr_6 thin film (film III), showing homogeneous Ti distribution, which is consistent with its phase-pure nature.

Based on these results, the proposed formation mechanism of the Cs_2TiBr_6 HP thin film is depicted schematically in Figure 1F. Here, the Ti^{4+} and Br^- are transported from the film top surface to the bottom of the film bottom via solid-state diffusion, resulting in the progression of the conversion-reaction front into the thin film. Owing to the compact nature of the initial CsBr thin film and the uniform $TiBr_4$ vapor atmosphere, no obvious in-plane reaction heterogeneity is observed in the thin film. We have further studied the effect of annealing temperature on the formation of the Cs_2TiBr_6 thin film. When a higher annealing temperature (230°C) is employed, the volatile $TiBr_4$ causes a high vapor pressure that immediately damages the CsBr thin film (see Figure S7), whereas when a lower-annealing temperature (150°C) is employed for the same annealing duration, Reaction 1 remains incomplete, resulting in the presence of CsBr in Cs_2TiBr_6 thin film (Figure S8). These results are consistent with the proposed diffusion-based film-formation mechanism. Thus, the annealing condition of 200°C for 24 hr is suitable for producing highly uniform and phase-pure Cs_2TiBr_6 HP thin films of ~200 nm thickness. The average grain size in this final Cs_2TiBr_6 HP thin film is ~270 nm, as measured using image analysis (see Figure S9), and the root-mean-square (RMS) roughness is 24.5 nm, as measured using atomic force microscopy (AFM) (Figure S10).

Favorable Optoelectronic Properties Unlock the Promise of Cs_2TiBr_6 for PSCs

For evaluating the potential of the as-fabricated Cs_2TiBr_6 thin films as a light-absorber material in PSCs, their optoelectronic properties that are closely related to the PV performance were measured. Figure 2A presents the Tauc plot and photoluminescence (PL) spectrum of the Cs_2TiBr_6 HP thin film. Linear fitting of the absorption band edge results in a bandgap of 1.82 eV, which is near ideal for top-cell application in tandem PVs with conventional Si-based or CIGS-based bottom cells.[23] Note that this bandgap is slightly higher than that of the Cs_2TiBr_6 HP bulk powder sample (1.78 eV).[21] The Cs_2TiBr_6 HP thin film also shows bright PL under excitation of 395-nm laser. The emission is centered at ~704 nm (1.76 eV), which is reasonably close to the bandgap. This first evidence of the PL properties of Cs_2TiBr_6 HP is of profound importance, as efficient PL is a hallmark of a good PV material. Figure 2B is a PL map of the Cs_2TiBr_6 HP thin film, showing highly uniform PL intensity over the whole film area. These results confirm the uniform physical properties of the as-deposited Cs_2TiBr_6 HP thin films over its entirety, which are highly consistent with the composition, phase, and microstructure uniformity results.

Photogenerated charge-carrier diffusion length in the light-absorber material in a PSC is another key optoelectronic property. To estimate the electron/hole diffusion

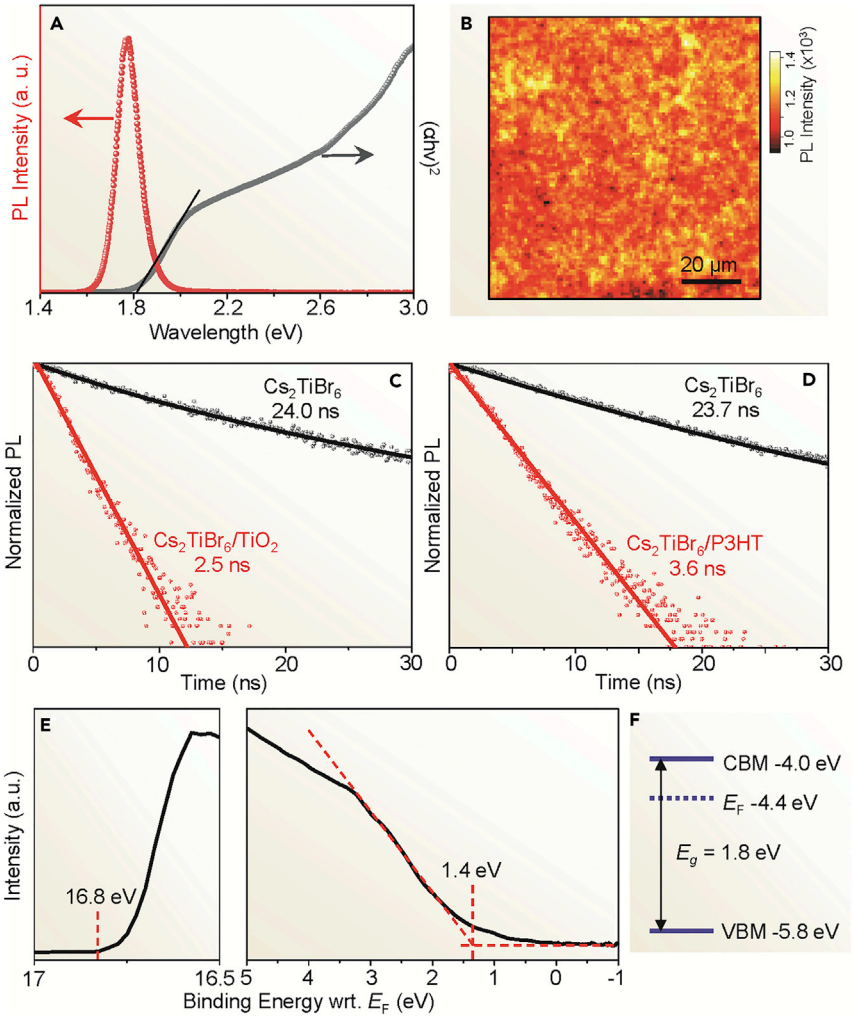

Figure 2. Optical and Band-Structure Properties of Cs_2TiBr_6 Thin Films

(A) Tauc plot and PL spectrum of the Cs_2TiBr_6 HP thin film.

(B–D) PL intensity map of the Cs_2TiBr_6 HP thin film (B). Time-resolved PL decay of the Cs_2TiBr_6 HP thin film: (C) with and without TiO_2 electron-quencher and (D) with and without P3HT hole-quencher.

(E) UPS spectrum of the Cs_2TiBr_6 HP thin film.

(F) Schematic illustration of the energy-level diagram of the Cs_2TiBr_6 HP thin film.

lengths in Cs_2TiBr_6, we studied the PL decay dynamics in the Cs_2TiBr_6 HP thin film with and without quencher layers. The PL spectra in Figure S11 confirm that TiO_2 and P3HT effectively quench the PL in the Cs_2TiBr_6 HP thin film and, thus, TiO_2 and P3HT were chosen as the electron- and hole-quenching layers, respectively. The distributions of photogenerated electrons or holes $n(x, t)$ in the Cs_2TiBr_6 thin film are described according to the following diffusion-based equation:[24]

$$\frac{\partial n(x,t)}{\partial t} = D\frac{\partial^2 n(x,t)}{\partial^2 t} - k(t)n(x,t), \qquad \text{Equation 1}$$

where D is the diffusion coefficient for electrons or holes and $k(t)$ is the PL decay rate, respectively. The $k(t)$, as a result of the total contribution from the monomolecular and bimolecular recombination, is determined by fitting a stretched exponential decay to the PL data measured from the bare Cs_2TiBr_6 HP thin film. Here, we assume that all the

photogenerated carriers that reach the TiO_2/Cs_2TiBr_6 or P3HT/Cs_2TiBr_6 interface will be quenched and, thus, the boundary conditions $n(L,t) = 0$ and $n(x,t) = n_o\exp(-Ax/L)$ are used, where $x = L$ means the interface of quencher/Cs_2TiBr_6 and A/L is the absorbance at 395 nm divided by Cs_2TiBr_6 thin film thickness. Finally, the characteristic diffusion lengths (L) of electrons and holes is calculated using[25]

$$L = \sqrt{D\tau}\,, \qquad \text{Equation 2}$$

where τ is the characteristic lifetime extracted at when the PL intensity falls to $1/e^{th}$ of its initial intensity without the quencher. Figure 2C shows time-resolved PL decay for a Cs_2TiBr_6 HP thin film with and without a TiO_2 quencher layer, where the extracted PL lifetimes are 24.0 ns and 2.5 ns, respectively. Using Equation 2, the L for electrons is estimated at 121 nm. Using the same method, the L for holes is estimated at 103 nm based on the results in Figure 2D. It is worth noting that the quencher (TiO_2 and P3HT) layers may not be ideal for Cs_2TiBr_6 HP and, thus, the above electron and hole diffusion length estimates are expected to be conservative. In this context, a solution-processed Spiro-OMeTAD layer was also tried as the hole-quencher layer, but it does not show better PL quenching than P3HT, as shown in Figure S12. This could be due to the fact that chlorobenzene solvent used for the deposition of the Spiro-OMeTAD layer damages the Cs_2TiBr_6 thin film. In this context, more accurate determination of the carrier-diffusion lengths in Cs_2TiBr_6 is a subject of our future research. Also, there are opportunities for optimizing the microstructures and compositions in the Cs_2TiBr_6 HP thin films for obtaining even longer diffusion lengths. Nevertheless, the estimated L values for electrons/holes here approach those found in the popular $MAPbI_3$ OIHP. Such long and balanced electron/hole diffusion lengths make the Cs_2TiBr_6 HP a new promising light-absorber material for planar-heterojunction PSCs.

We have calculated the band structure and density of states (DOS) of Cs_2TiBr_6, which reveals the quasi-direct nature of the bandgap of Cs_2TiBr_6. As shown in Figure S13, Cs_2TiBr_6 possesses an indirect fundamental bandgap between Γ (valence band maximum, VBM) and X (conduction band minimum, CBM) and a direct bandgap at X, slightly larger than the indirect gap by ~30 meV. An analysis of the orbital character of Cs_2TiBr_6 reveals that the highest valence band levels are contributed mostly by the Br 4*p* orbital, while the lowest conduction band levels are contributed by the Ti 3*d* orbital at Γ and X points. The isotropic electron and hole effective masses at the X and Γ points are also computed, respectively. The holes have both light and heavy effective masses, $-0.9\ m_e$ and $-1.79\ m_e$, respectively, at Γ point. The electrons have effective mass of $1.79\ m_e$. The quasi-direct nature of the bandgap and the relatively low effective masses of carriers in Cs_2TiBr_6 are consistent with the outstanding charge-carrier diffusion. Note that the calculated effective mass of electrons can be heavier than that of holes, which could be due to the limitations of our DFT calculations that use only the PBE functional. Comprehensive understanding of the electronic structure of the Ti-based HP materials is presented in our parallel study.[21]

The intrinsically favorable optoelectronic properties are not enough for qualifying the Cs_2TiBr_6 HP thin film as a good PV material. Since solar cells are multi-component devices, it is necessary that the energy levels of the candidate PV materials match well with the other layers in the solar cell device, such as the electron-transporting layer (ETL) and hole-transporting layer (HTL). To this end, we determined the CBM and VBM energy levels using UV photoelectron spectroscopy (UPS), and the results are presented in Figure 2E. The 4.5-eV work function of Cs_2TiBr_6 HP was calculated by subtracting the cutoff (16.75 eV) located in the higher

binding-energy region from the energy of He ions (21.2 eV).[26–28] The turning point located at the lower binding-energy region indicates the energy gap between the VBM energy level and Fermi level of Cs_2TiBr_6 HP. Thus, the VBM is estimated at −5.9 eV for the Cs_2TiBr_6 thin film with respect to the vacuum energy level. Correspondingly, the CBM energy level was deduced to be −4.1 eV based on the optical bandgap (1.82 eV) of the Cs_2TiBr_6 thin film. It can also be seen that the Fermi level of the Cs_2TiBr_6 thin film is relatively closer to the CBM, indicative of the *n*-type self-doping nature of the as-prepared Cs_2TiBr_6 HP thin film. The energy-level diagram is shown schematically in Figure 2F. The VBM/CBM values match favorably with the state-of-the-art ETL materials (e.g., TiO_2, C_{60}) and HTL materials (e.g., Spiro-OMeTAD, PEDOT, P3HT, NiO) that are widely used in PSCs. This offers many possibilities for developing Cs_2TiBr_6-based PSCs with several different device architectures for achieving optimal PV performance.

Device Design Boosts the Efficiency of Cs_2TiBr_6 PSCs

To evaluate the PV performance of the Cs_2TiBr_6 thin film, we fabricated PSCs by sandwiching the Cs_2TiBr_6 thin film between a TiO_2 ETL and a P3HT HTL. Fluorine-doped tin oxide (FTO) and Au are used as the electrodes. The schematic illustrations of this PSC device architecture and the energy-level diagram are shown in Figures 3A and 3B, respectively. The current density-voltage (*J-V*) curves of this PSC in both forward and reverse scans are shown in Figure 3C, and the extracted PV performance parameters are presented in Table 1. The PSC shows a respectable overall PCE of 2.26% in reverse scan with small hysteresis (2.05% in forward scan). The stabilized PCE output is 2.15% at the maximum power point, which is reached immediately upon light illumination as shown in Figure 3D. This efficient photoresponse is mainly contributed by Cs_2TiBr_6 rather than P3HT, as the P3HT layer has negligible contribution to light absorption in our devices (see Figure S14). We have further probed the photoresponse of Cs_2TiBr_6 HP using conductive AFM under light. As shown in Figure S15, compared with P3HT, Cs_2TiBr_6 shows more than an order-of-magnitude higher photocurrent, which confirms that the measured PCE is mainly attributed to the Cs_2TiBr_6 HP thin film in our device. This attests to the role of Cs_2TiBr_6 HP as an efficient light-absorber material. Admittedly, 2.26% PCE is quite low for the practical PV applications. In this context, we further demonstrate the feasibility of improving the performance of the PSCs by incorporating a C_{60} interfacial layer between the Cs_2TiBr_6 HP thin film and the TiO_2 ETL. The overall PCE is improved to a maximum 3.28% in reverse scan (Figure 3C and Table 1). The stabilized PCE output at the maximum power point is 3.22% (Figure 3D). The external quantum efficiency (EQE) spectrum of the same PSC shows an integrated current density (5.43 $mA.cm^{-2}$), which is close to the short-circuit current density (J_{SC}) extracted from the *J-V* curves in Figure 3C (Table 1). The EQE spectrum shows a band edge at ~680 nm, which is identical to the absorption edge shown in Figure 2A. Figure 3F presents the PCE statistics of the Cs_2TiBr_6 thin film-based PSC with the C_{60} interfacial layer, which shows a tight PCE distribution with a mean value of 3%.

It is useful to understand the origin of the PV performance enhancement with the C_{60} interfacial layer, as it could provide guidelines for the future development of more efficient PSCs based on Cs_2TiBr_6 HP thin films. Here, we have found that the C_{60} interfacial layer has two beneficial functions. First, as shown in Figure 3B, C_{60} molecules have a CBM commensurate with that of TiO_2 ETL and Cs_2TiBr_6 HP, which can facilitate the electron transfer from Cs_2TiBr_6 to the TiO_2 ETL. This is consistent with the fact that the PL is much more efficiently quenched with the presence of C_{60} (Figure S11). Second, the C_{60} layer influences the microstructure of the as-deposited CsBr thin film and, thus, the formation of the Cs_2TiBr_6 HP thin film. As seen in Figure S16, with

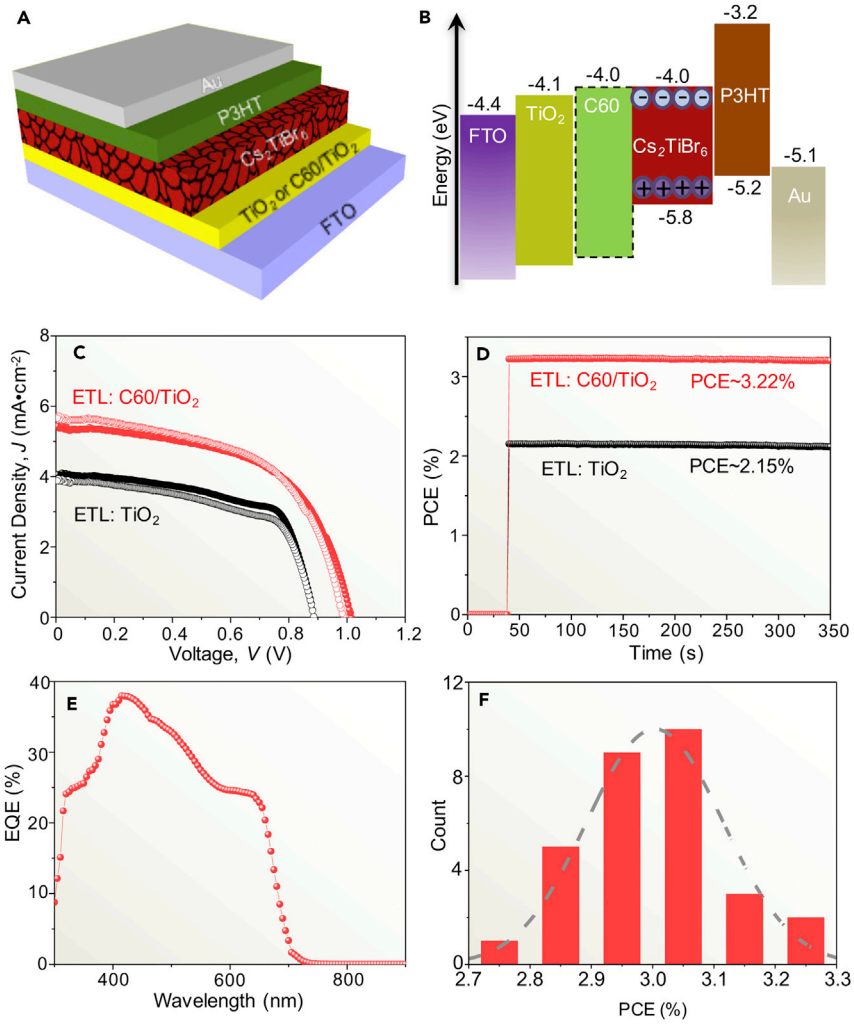

Figure 3. Structure, Properties, and Performance of Solar Cells Based on Cs_2TiBr_6 Thin Films

(A and B) Schematic illustrations of (A) PSC architecture using the Cs_2TiBr_6 HP thin film as the light absorber and (B) energy levels in the PSC.

(C) *J-V* curves at both forward (hollow circles) and reverse (solid circles) scans of the best PSCs without and with the presence of the C_{60} interfacial layer.

(D) Stabilized PCE output at the maximum power points of the PSCs without and with the presence of the C_{60} interfacial layer.

(E) EQE spectrum of the best PSC with the presence of the C_{60} interfacial layer.

(F) PCE statistics of the PSC with the presence of the C_{60} interfacial layer.

the incorporation of the C_{60} layer, the as-deposited CsBr thin film under the same preparation conditions exhibits a reduced grain size and a higher-density grain-boundary network. This modified CsBr microstructure facilitates Reaction 1, most likely due to the faster through-thickness ion diffusion along the grain boundaries. It is found that the Reaction 1 completion time is reduced by half (12 hr) in this case. As a result, the final Cs_2TiBr_6 HP thin film shows superior quality with a reduced RMS roughness of 14.6 nm (Figure S17). These findings point to clear directions for improving the Cs_2TiBr_6-based PSCs through device and film-microstructure engineering strategies. While we have demonstrated the proof of concept of PSC devices based on Cs_2TiBr_6 HP thin films and the possible strategies for improving them, the achieved best PCE exceeds several of the PCEs of PSCs based on other Pb-free HPs.[16,20,29] In particular, the best V_{OC}

Table 1. PV Performance Parameters of PSCs Based on Cs_2TiBr_6 with and without C_{60}

	Scan Direction	V_{OC} (V)	J_{SC} (mA.cm^{-2})	FF	PCE (%)	Stable PCE (%)
Cs_2TiBr_6 with C_{60}	Reverse	1.02	5.69	0.564	3.28	3.22
	Forward	0.99	5.75	0.549	3.12	
Cs_2TiBr_6	Reverse	0.89	4.03	0.631	2.26	2.15
	Forward	0.89	3.87	0.595	2.05	

achieved here is over 1.0 V, which shows the great potential of the Cs_2TiBr_6 HP thin film for PSCs. For comparison, the most widely studied all-inorganic Sn-based Pb-free HPs show a V_{OC} less than 0.6 V.[30,31]

Cs_2TiBr_6 PSCs Are Intrinsically/Environmentally Stable

Intrinsic and environmental stability of the Cs_2TiBr_6 HP thin films have also been assessed. Thermogravimetric analysis (TGA) results in Figure S18 show that the decomposition of Cs_2TiBr_6 starts at a temperature as high as 400°C. For comparison, the popular $MAPbI_3$, $MAPbBr_3$, and $MASnI_3$ OIHPs begin to decompose at 330°C, 340°C, and 200°C, respectively.[32–34] This is attributed to the all-inorganic nature of the Cs_2TiBr_6 HP, and that the titanium cation exists in its preferred and stable +4 oxidation state. Note that, unlike other titanium halides such as $TiCl_4$, Cs_2TiBr_6 is not susceptible to the ambient degradation and conversion to titania. The environmental stability of the Cs_2TiBr_6 HP thin films was further tested by examining their tolerance to heat, moisture, and light. A uniform $MAPbI_2Br$ OIHP was used as the reference film, as it exhibits nearly the same bandgap as Cs_2TiBr_6, and it is the most popular choice for use in PSCs for tandem PV applications. We also note here that Pb-based HPs, in general, have higher environmental stability compared with their Pb-free counterparts.[35,36] The heat-tolerance experiment was conducted by annealing the film at 200°C for 6 hr in an N_2-filled glovebox. The moisture tolerance was tested by storing the film in a precisely controlled climate chamber (23°C, 80% relative humidity [RH], 6 hr). The tolerance of the film to sunlight was evaluated by placing the film under stimulated one-sun illumination for 24 hr where the film is sealed with a poly(methyl methacrylate) coating to exclude other environmental effects. These test conditions are intended to isolate the thermal, moisture, and light effects. The Cs_2TiBr_6 HP thin films used in these tests were all deposited on compact TiO_2-coated glass substrates, bearing in mind that the TiO_2-perovskite interfaces are regarded as an important factor in PSC device stability. By comparing the XRD patterns from the thin films before and after being subjected to environmental (heat/moisture/light) stresses in Figures 4A and 4B, it is concluded that the Cs_2TiBr_6 HP thin films show much higher tolerance compared with the reference thin film, which degrades to PbI_2. Note that, while the time duration chosen to evaluate environmental stresses is until significant degradation occurs in the reference film, the Cs_2TiBr_6 thin films can maintain their phase purity for much longer durations. For example, in the thermal stability test, when the annealing time is prolonged to 24 hr, there is still no obvious degradation (Figure S19). These results clearly confirm the superior intrinsic/environmental stability of Cs_2TiBr_6 HP thin films.

In additional experiments, the PCE evolution of the PSC device (unencapsulated) was monitored as a function of its storage time (70°C, 30% RH, ambient light). As seen in Figure 4D, after 14 days of storage the PSC still shows a PCE of 3.03% (94% PCE retention). We have further evaluated the stability of the PSC device (unencapsulated) under continuous one-sun illumination, which still shows good PCE retention of 85% (Figure S20). While more standard PSC stability testing is

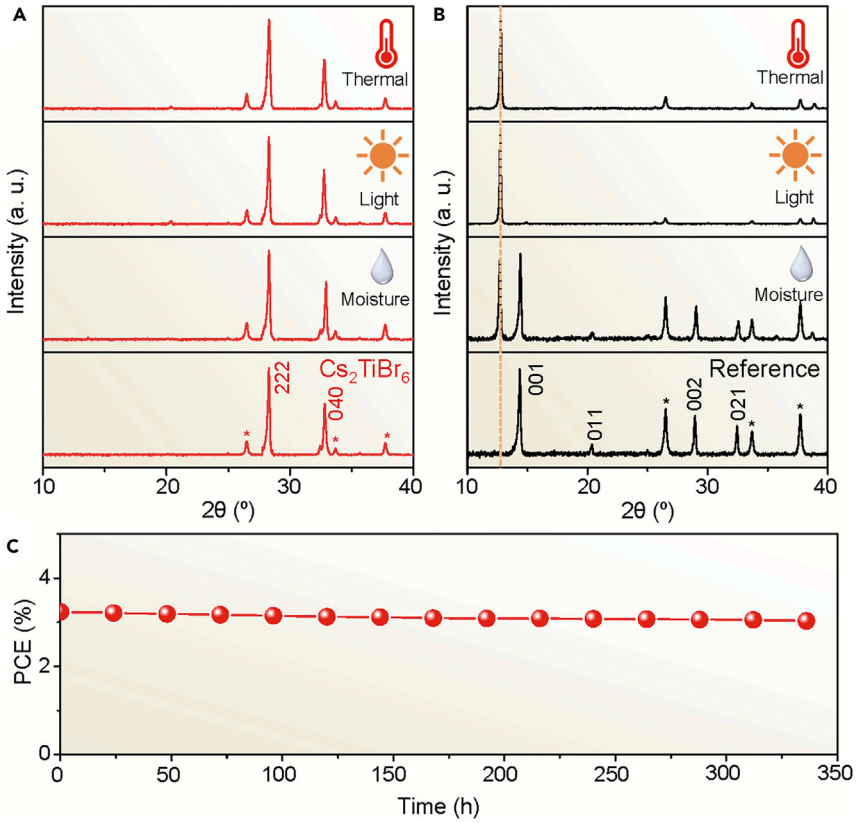

Figure 4. Stability of Solar Cells Gased on Cs_2TiBr_6 Thin Films

(A and B) XRD patterns of before (bottom) and after heat (200°C, 6 hr, N_2 atmosphere), light (one-sun, encapsulated), and moisture (23°C, 80% RH, 6 hr) stresses: (A) Cs_2TiBr_6 HP thin film and (B) Reference $MAPbI_2Br$ OIHP thin film (vertical dashed line indicates main PbI_2 peak). * Indicates FTO substrate peak.

(C) Evolution of PCE of the best Cs_2TiBr_6-based PSC (unencapsulated) as function of the storage time under environmental stress (70°C, 30% RH, ambient light).

expected to be performed in the future, these results show the promise of Cs_2TiBr_6 HP thin films for stable PSCs.

In closing, we have demonstrated that phase-pure, uniform Cs_2TiBr_6 HP thin films can be synthesized via a two-step vapor deposition method, wherein a diffusion-based mechanism is at play. The as-deposited Cs_2TiBr_6 HP thin films show a favorable bandgap of 1.82 eV, with uniform PL. The photogenerated carrier-diffusion lengths for electrons and holes are balanced, and are at least 121 nm and 103 nm, respectively. Planar-heterojunction PSCs fabricated using the Cs_2TiBr_6 HP thin films show PCE of up to 3.3%. The insertion of a C_{60} layer between the Cs_2TiBr_6 HP thin film and the TiO_2 ETL results in the enhancement of the PCE, showing that device and film-microstructure engineering strategies can be used to further boost the PSC PCEs. The Cs_2TiBr_6 HP thin films and the resulting PSCs are highly stable under key environmental stresses of heat, moisture, and light. This first study on the new Pb-free Ti-based PSCs may lead to a new research paradigm in exploring environmentally friendly and stable solar cells of the future. It is also envisioned that composition engineering of Cs_2TiBr_6 HP thin films, such as iodide[21] or chloride alloying, will lead to the discovery of a broader family of Ti-based HPs with controlled bandgaps and properties for a wide range of optoelectronic applications.

EXPERIMENTAL PROCEDURES

Materials and Thin Film Synthesis

All the raw chemicals were purchased from Sigma-Aldrich (USA) and used as received. For the fabrication of the Cs_2TiBr_6 HP thin films, a CsBr layer of thickness ~100 nm was first deposited on the substrate by thermal evaporation. The as-deposited CsBr thin film was placed in a home-made chamber (see Figure S1) filled with $TiBr_4$ vapor. The $TiBr_4$ vapor was slowly generated by heating $TiBr_4$ powder at 200°C. The typical reaction time for the complete conversion of CsBr to pure-phase Cs_2TiBr_6 is 24 hr when a TiO_2/FTO-glass substrate is used, as discussed in the main text. The resulting Cs_2TiBr_6 thin films were washed using toluene to remove any possible excess $TiBr_4$ on the film surface for subsequent characterization and device fabrication.

Materials Characterization

XRD of the thin films was performed using a high-resolution diffractometer (D8 Advance; Bruker, Germany) with CuK_α radiation. UV-vis spectra were obtained using a spectrophotometer (UV-2600; Shimadzu, Japan). The morphology and EDS elemental-distribution maps of the thin film were observed in a scanning electron microscope (LEO 1530VP; Carl Zeiss, Germany) equipped with an EDS detector (Oxford Instruments, UK). The FIB (Helios 600; FEI, Hillisboro, OR) was used to etch the thin films, where the different depths were achieved by Ga^+ ion bombardment. A PHI5600 XPS system was used to acquire both XPS and UPS spectra. The analysis chamber base pressures were $<1 \times 10^{-9}$ torr prior to analysis. The instrument utilized a monochromated K_α Al source for X-ray radiation at 1,486.7 eV, and a UVS 40A2 (PREVAC, Poland) UV source and UV40A power supply provided by He 1α excitation (He I) for UPS at 21.22 eV. Chamber pressure for UPS was maintained at $<3 \times 10^{-8}$ torr. The steady-state and time-resolved PL spectra were recorded with a Varian Cary Eclipse fluorescence spectrophotometer operating at 395 nm excitation. The decay rate and lifetime was determined using the two-parameter decay function fitting method (Equation 1). The fitted diffusion coefficients for electrons and holes in Equation 1 are 0.61 $cm^2\ s^{-1}$ and 0.44 $cm^2\ s^{-1}$, respectively, which are used to calculate the corresponding diffusion lengths using Equation 2. The *pc*-AFM measurements were conducted in contact mode using an MFP-3D AFM (Asylum Research, USA) with a conducting platinum-coated silicon probe (Econo-SCM-PIC, Asylum Research) and an LED light source.

DFT Computations

All first-principles computations are performed based on density functional theory (DFT) methods as implemented in the Vienna *ab initio* simulation package (VASP 5.4; see Ju et al.[21] for details). Briefly, an energy cutoff of 520 eV is employed, and the atomic positions are optimized using the conjugate gradient scheme without any symmetric restrictions until the maximum force on each atom is less than 0.02 eV $Å^{-1}$. The ion cores are described using the projector augmented wave method. Grimme's long-range van der Waals interaction is described using DFT-D3 correction. A 16 × 16 × 16 k-point grid is used.

Solar Cell Fabrication and Testing

For the fabrication of PSCs, a compact-TiO_2 ETL was first deposited on pre-patterned FTO-coated glass by spray pyrolysis at 450°C. For some PSCs, an interfacial layer of C_{60} layer was deposited before the deposition of the Cs_2TiBr_6 thin film. This C_{60} layer was deposited by spin-coating a solution of C_{60} in chlorobenzene (2 mg/mL) at 3,000 rpm for 40 s on the as-prepared TiO_2 substrate, followed by annealing at 100°C for 30 min. The Cs_2TiBr_6 thin film was then deposited based on the procedure described above, followed by spin-coating the HTL solution, which

consisted of 10 mg P3HT and 1 mL of toluene solvent. Finally, the Au layer was deposited using a thermal evaporator and a shadow mask. The *J-V* characteristics of the PSCs were measured using a 2400 SourceMeter (Keithley, USA) under simulated one-sun AM1.5G 100 $mW.cm^{-2}$ intensity (Sol3A Class AAA; Oriel, Newport, USA), under both reverse (from V_{OC} to J_{SC}) and forward (from J_{SC} to V_{OC}) scans. The step voltage was 5 mV with a 10-ms delay time per step. The maximum-power output stability of PSCs was measured by monitoring the *J* output at the maximum-power-point *V* bias (deduced from the reverse-scan *J-V* curves) using the 2400 SourceMeter. A typical active area of 0.12 cm^2 was defined using a non-reflective mask for the *J-V* measurements. The stable output PCE was calculated using the following relation: PCE = *J* ($mA.cm^{-2}$) × *V* (V)/100 ($mW.cm^{-2}$). A shutter was used to control the one-sun illumination on the PSC. The EQE spectra were obtained using a quantum efficiency measurement system (IQE 200B; Oriel) consisting of a xenon lamp, a monochromator, a lock-in amplifier, and a calibrated silicon photodetector. The PSC stability was evaluated by measuring the *J-V* characteristics of PSCs after storing the cells under constant environmental stress for a certain period of time in an environmental climate chamber (HPP110; Memmert, Germany).

SUPPLEMENTAL INFORMATION

Supplemental Information includes 20 figures and can be found with this article online at https://doi.org/10.1016/j.joule.2018.01.009.

ACKNOWLEDGMENTS

This research is supported by the National Science Foundation (no. OIA-1538893). M.G.J. and X.C.Z. acknowledge additional support from NSF (no. DMR-1420645).

AUTHOR CONTRIBUTIONS

M.C., M.-G.J., X.C.Z., Y. Zhou, and N.P.P. conceived the idea. M.C., Y. Zhou, and N.P.P. designed the experiments. M.C. conducted the synthesis and characterization experiments. A.D.C. and R.L.G. conducted the UPS and XPS experiments. J.G. conducted the PL experiments. M.C. performed the solar cell fabrication and testing. Y. Zong helped with the light-stability testing and materials characterization. All the authors contributed to the analysis of the data and the writing of the manuscript.

DECLARATION OF INTERESTS

We have filed a provisional patent related to this work: Application No. 62564596, dated September 28, 2017.

Received: November 11, 2017
Revised: December 23, 2017
Accepted: January 18, 2018
Published: February 13, 2018

REFERENCES

1. Kojima, A., Teshima, K., Shirai, Y., and Miyasaka, T. (2009). Organometal halide perovskites as visible-light sensitizers for photovoltaic cells. J. Am. Chem. Soc. *131*, 6050–6051.

2. Yang, W.S., Park, B.W., Jung, E.H., Jeon, N.J., Kim, Y.C., Lee, D.U., Shin, S.S., Seo, J., Kim, E.K., Noh, J.H., and Seok, S.I. (2017). Iodide management in formamidinium-lead-halide–based perovskite layers for efficient solar cells. Science *356*, 1376–1379.

3. Kim, H.S., Lee, C.-R., Im, J.H., Lee, K.B., Moehl, T., Marchioro, A., Moon, S.J., Humphry-Baker, R., Yum, J.H., Moser, J.E., et al. (2012). Lead iodide perovskite sensitized all-solid-state submicron thin film mesoscopic solar cell with efficiency exceeding 9%. Sci. Rep. *2*, 591.

4. Eperon, G.E., Leijtens, T., Bush, K.A., Prasanna, R., Green, T., Wang, J.T.-W., McMeekin, D.P., Volonakis, G., Milot, R.L., May, R., et al. (2016). Perovskite-perovskite tandem photovoltaics with optimized band gaps. Science *354*, 861–865.

5. Tan, H., Jain, A., Voznyy, O., Lan, X., García de Arquer, F.P., Fan, J.Z., Quintero-Bermudez, R., Yuan, M., Zhang, B., Zhao, Y., et al. (2017). Efficient and stable solution-processed planar perovskite solar cells via contact passivation. Science *355*, 722–726.

6. Chen, B., Zheng, X., Bai, Y., Padture, N.P., and Huang, J. (2017). Progress in tandem solar cells based on hybrid organic-inorganic perovskites. Adv. Energy Mater. *7*, 1602400.

7. Green, M.A., Ho-Baillie, A., and Snaith, H.J. (2014). The emergence of perovskite solar cells. Nat. Photonics *8*, 506–514.

8. Zhou, Y., Zhou, Z., Chen, M., Zong, Y., Huang, J., Pang, S., and Padture, N.P. (2016). Doping and alloying for improved perovskite solar cells. J. Mater. Chem. A *4*, 17623–17635.

9. Giustino, F., and Snaith, H.J. (2016). Toward lead-free perovskite soar cells. ACS Energy Lett. *1*, 1233–1240.

10. Noel, N.K., Stranks, S.D., Abate, A., Wehrenfennig, C., Guarnera, S., Haghighirad, A.-A., Sadhanala, A., Eperon, G.E., Pathak, S.K., Johnston, M.B., et al. (2014). Lead-free organic-inorganic tin halide perovskites for photovoltaic applications. Energy Environ. Sci. *7*, 3061–3068.

11. Yang, Y., and You, J. (2017). Make perovskite solar cell stable. Nature *544*, 155–156.

12. Rong, Y., Liu, L., Mei, A., Li, X., and Han, H. (2015). Beyond efficiency: the challenge of stability in mesoscopic perovskite solar cells. Adv. Energy Mater. *5*, 1501066.

13. Abate, A. (2017). Perovskite solar cells go lead free. Joule *1*, 659–664.

14. Chung, I., Song, J.-H., Im, J., Androulakis, J., Malliakas, C.D., Li, H., Freeman, A.J., Kenney, J.T., and Kanatzidis, M.G. (2012). $CsSnI_3$: semiconductor or metal? High electrical conductivity and strong near-infrared photoluminescence from a single material. high hole mobility and phase-transitions. J. Am. Chem. Soc. *134*, 8579–8587.

15. Wang, N., Zhou, Y., Ju, M.-G., Garces, H.F., Ding, T., Pang, S., Zeng, X.C., Padture, N.P., and Sun, X.W. (2016). Heterojunction-depleted lead-free perovskite solar cells with coarse-grained B-γ-$CsSnI_3$ thin films. Adv. Energy Mater. *6*, 1601130.

16. Marshall, K.P., Walker, M., Walton, R.I., and Hatton, R.A. (2016). Enhanced stability and efficiency in hole-transport-layer-free $CsSnI_3$ perovskite photovoltaics. Nat. Energy *1*, 16178.

17. Babayigit, A., Ethirajan, A., Muller, M., and Conings, B. (2016). Toxicity of organometal halide perovskite solar cells. Nat. Mater. *15*, 247–251.

18. Saparov, B., Hong, F., Sun, J.-P., Duan, H.-S., Meng, W., Cameron, S., Hill, I.G., Yan, Y., and Mitzi, D.B. (2015). Thin-film preparation and characterization of $Cs_3Sb_2I_9$: a lead-free layered perovskite semiconductor. Chem. Mater. *27*, 5622–5632.

19. Du, K.-Z., Meng, W., Wang, X., Yan, Y., and Mitzi, D.B. (2017). Bandgap engineering of lead-free double perovskite $Cs_2AgBiBr_6$ through trivalent metal alloying. Angew. Chem. Int. Ed. *56*, 8158–8162.

20. Park, B.W., Philippe, B., Zhang, X., Rensmo, H., Boschloo, G., and Johansson, E.M.J. (2015). Bismuth based hybrid perovskites $A_3Bi_2I_9$ (A: methylammonium or cesium) for solar cell application. Adv. Mater. *27*, 6806–6813.

21. Ju, M.-G., Chen, M., Zhou, Y., Graces, H.F., Dai, J., Ma, L., Padture, N.P., and Zeng, X.C. (2018). Earth-abundant non-toxic titanium (IV) based vacancy-ordered double perovskite halides with tunable 1.0 to 1.8 eV bandgaps for photovoltaic applications. ACS Energy Lett. *3*, 297–304.

22. Gálfi, L., and Rácz, Z. (1988). Properties of the reaction front in an A+B-C type reaction-diffusion process. Phys. Rev. A. *38*, 3151–3154.

23. McMeekin, D.P., Sadoughi, G., Rehman, W., Eperon, G.E., Saliba, M., Hörantner, M.T., Haghighirad, A., Sakai, N., Korte, L., Rech, B., et al. (2016). A mixed-cation lead mixed-halide perovskite absorber for tandem solar cells. Science *351*, 151–155.

24. Stranks, S.D., Eperon, G.E., Grancini, G., Menelaou, C., Alcocer, M.J.P., Leijtens, T., Herz, L.M., Petrozza, A., and Snaith, H.J. (2013). Electron-hole diffusion lengths exceeding 1 micrometer in an organometal trihalide perovskite absorber. Science *342*, 341–344.

25. Chen, M., Gu, J., Sun, C., Zhao, Y., Zhang, R., You, X., Liu, Q., Zhang, W., Su, Y., Su, H., et al. (2016). Light-driven overall water splitting enabled by a photo-dember effect realized on 3D plasmonic structures. ACS Nano *10*, 6693–6701.

26. Wang, J., Qin, M., Tao, H., Ke, W., Chen, Z., Wan, J., Qin, P., Xiong, L., Lei, H., Yu, H., et al. (2015). Performance enhancement of perovskite solar cells with Mg-doped TiO_2 compact film as the hole-blocking layer. Appl. Phys. Lett. *106*, 121104.

27. Liu, J., Gao, C., Luo, L., Ye, Q., He, X., Ouyang, L., Guo, X., Zhuang, D., Liao, C., Mei, J., and Lau, W. (2015). Low-temperature, solution processed metal sulfide as an electron transport layer for efficient planar perovskite solar cells. J. Mater. Chem. A *3*, 11750–11755.

28. Sakai, N., Haghighirad, A.A., Filip, M.R., Nayak, P.K., Nayak, S., Ramadan, A., Wang, Z., Giustino, F., and Snaith, H.J. (2017). Solution-processed cesium hexabromopalladate (IV), Cs_2PdBr_6, for optoelectronic applications. J. Am. Chem. Soc. *139*, 6030–6033.

29. Greul, E., Petrus, M., Binek, A., Docampo, P., and Bein, T. (2017). Highly stable, phase pure $Cs_2AgBiBr_6$ double perovskite thin films for optoelectronic applications. J. Mater. Chem. A *5*, 19972–19981.

30. Hao, F., Stoumpos, C.C., Cao, D.H., Chang, R.P.H., and Kanatzidis, M.G. (2014). Lead-free solid-state organic-inorganic halide perovskite solar cells. Nat. Photonics *8*, 489–494.

31. Ke, W., Stoumpos, C.C., Zhu, M., Mao, L., Spanopoulos, I., Liu, J., Kontsevoi, O.Y., Chen, M., Sarma, D., Zhang, Y., et al. (2017). Enhanced photovoltaic performance and stability with a new type of hollow 3D perovskite {en}$FASnI_3$. Sci. Adv. *3*, e1710293.

32. Dang, Y., Zhou, Y., Liu, X., Ju, D., Xia, S., Xia, H., and Tao, X. (2016). Formation of hybrid perovskite tin iodide single crystals by top-seeded solution growth. Angew. Chem. Int. Ed. *55*, 3447–3450.

33. Dang, Y., Liu, Y., Sun, Y., Yuan, D., Liu, X., Lu, W., Liu, G., Xia, H., and Tao, X. (2015). Bulk crystal growth of hybrid perovskite material $CH_3NH_3PbI_3$. CrystEngComm *17*, 665–670.

34. Brunetti, B., Cavallo, C., Ciccioli, A., Gigli, G., and Latini, A. (2016). On the thermal and thermodynamic (in)stability of methylammonium lead halide perovskites. Sci. Rep. *6*, 31896.

35. Grätzel, M. (2014). The light and shade of perovskite solar cells. Nat. Mater. *13*, 838–842.

36. Leijtens, T., Eperon, G.E., Noel, N.K., Habisreutinger, S.N., Petrozza, A., and Snaith, H.J. (2015). Stability of metal halide perovskite solar cells. Adv. Energy Mater. *5*, 1500963.

JOUL, Volume *2*

Supplemental Information

Cesium Titanium(IV) Bromide Thin Films Based Stable Lead-free Perovskite Solar Cells

Min Chen, Ming-Gang Ju, Alexander D. Carl, Yingxia Zong, Ronald L. Grimm, Jiajun Gu, Xiao Cheng Zeng, Yuanyuan Zhou, and Nitin P. Padture

Supplemental Information

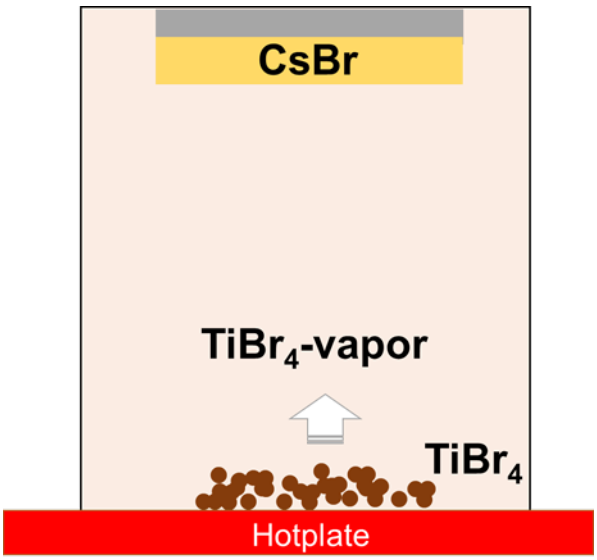

Figure S1. Schematic illustration of the experimental setup for reacting as-deposited CsBr thin film on a substrate with $TiBr_4$ vapor for conversion to phase-pure Cs_2TiBr_6 HP thin film.

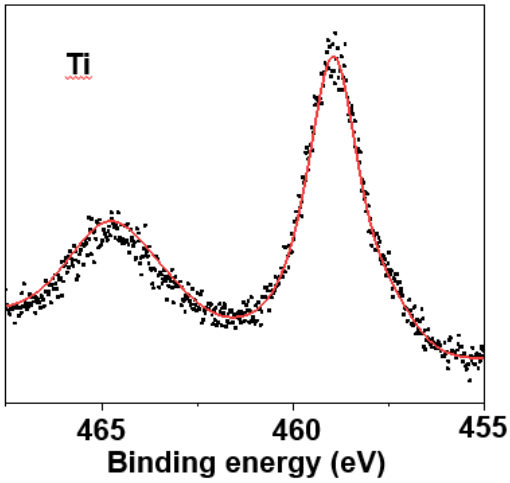

Figure S2. XPS spectrum for Ti 2*p* in an as-prepared Cs_2TiBr_6 HP thin film.

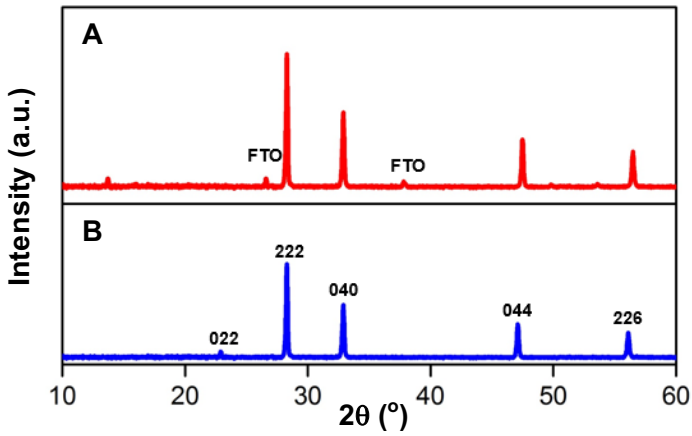

Figure S3. XRD patterns of the Cs_2TiBr_6 HP: (A) thin film (red) and (B) bulk powder (control sample; blue).

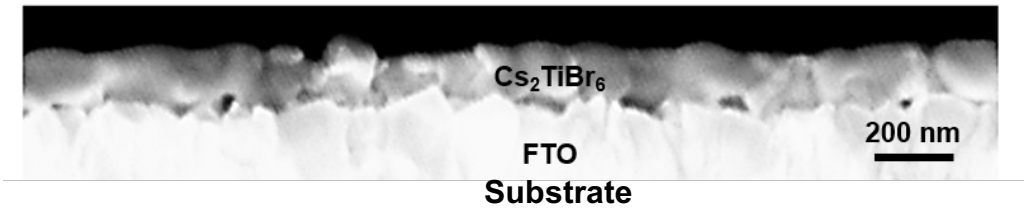

Figure S4. A typical cross-sectional SEM micrograph of the in the Cs_2TiBr_6 HP thin film.

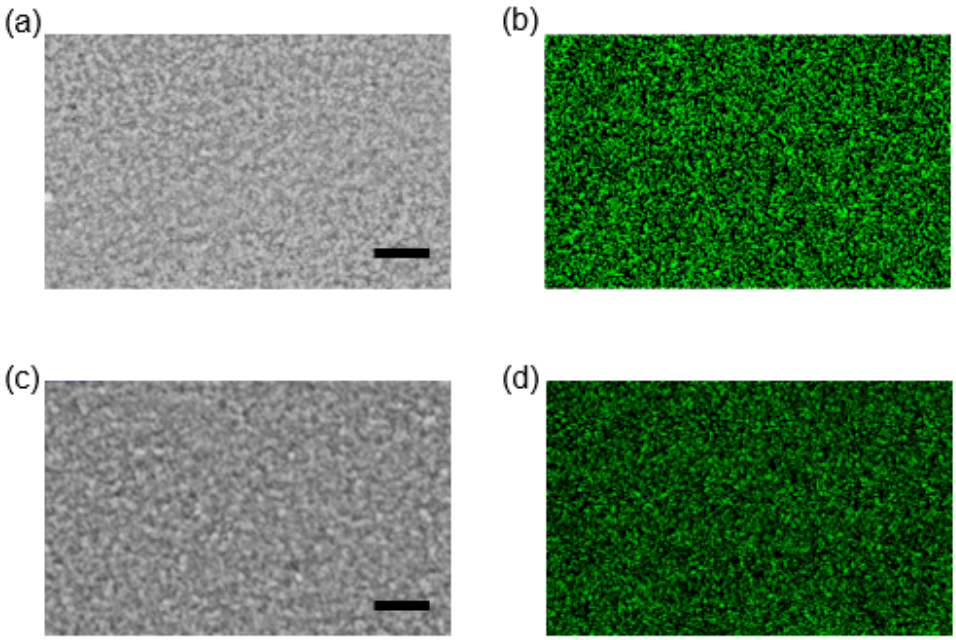

Figure S5. Surface morphology at: (a) top surface and (c) 40 nm from top surface of the intermediate Film-II. Corresponding EDS Ti elemental maps of Ti: (b) top surface and (d) 40 nm from film top surface. Scale bars = 5 μm.

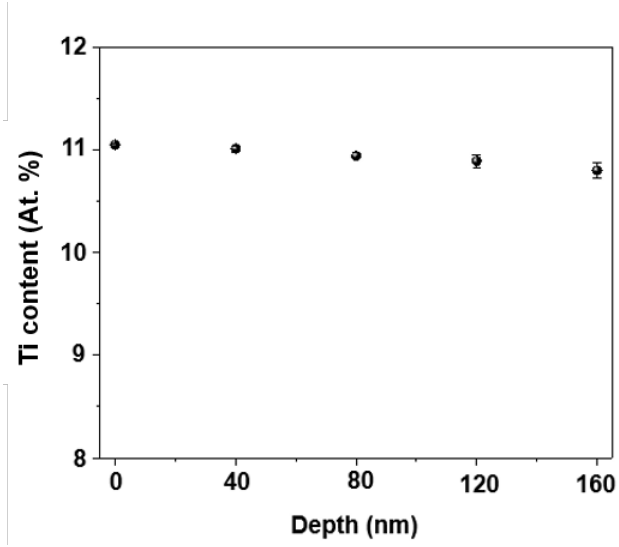

Figure S6. Ti content as a function of depth in the Cs_2TiBr_6 HP thin film after 24-h annealing at 200 ˚C (Film-III).

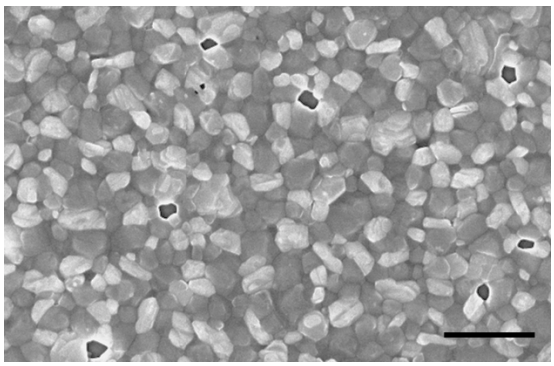

Figure S7. Surface morphology for the thin film annealed at a higher temperature (230 ˚C) for 24 h. Scale bar = 1 μm.

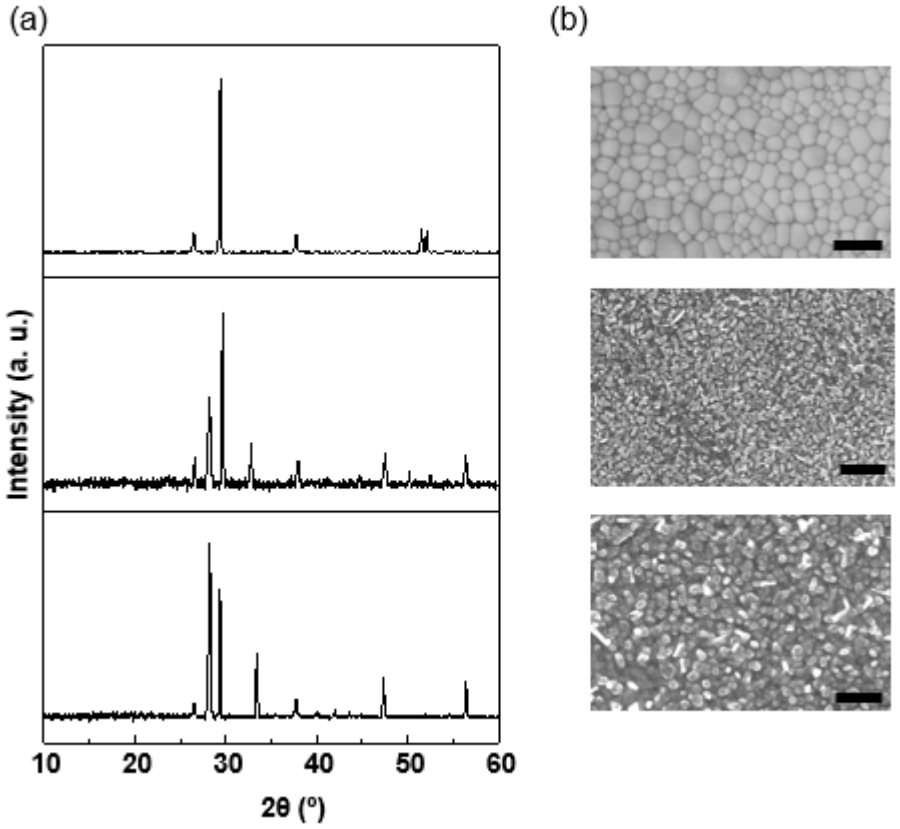

Figure S8. (a) XRD patterns and (b) corresponding SEM micrographs of top surfaces of thin films annealed at a lower temperature (150 ˚C) for: as-deposited CsBr thin film (top), 12 h (middle), and 24 h (bottom). Scale bars = 1 μm.

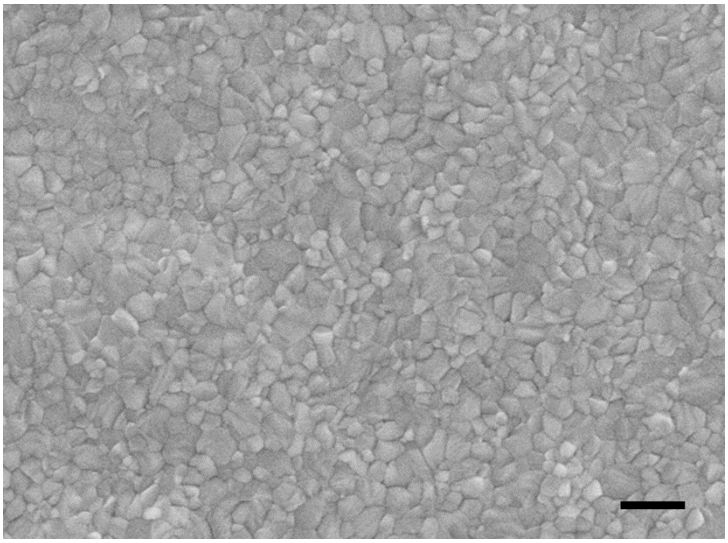

Figure S9. SEM image of top surface of a Cs_2TiBr_6 HP thin film used for estimating the average grain size employing image analysis. Scale bar = 1 μm.

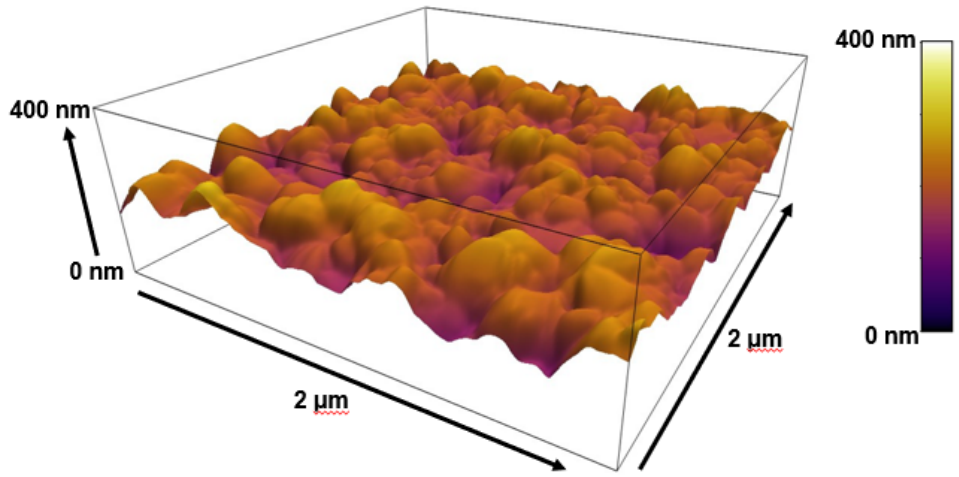

Figure S10. AFM scan of top-surface of a Cs_2TiBr_6 HP thin film on TiO_2-coated glass substrate.

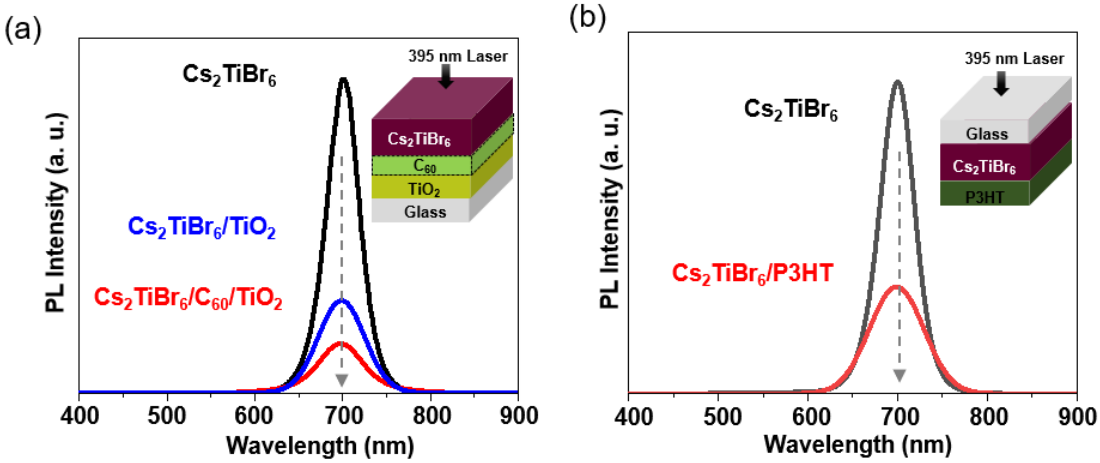

Figure S11. PL spectra from: (a) Cs_2TiBr_6/glass, Cs_2TiBr_6/TiO_2/glass, and Cs_2TiBr_6/C60/TiO_2/glass and (b) glass/Cs_2TiBr_6 and glass/Cs_2TiBr_6/P3HT. Insets: schematic illustrations of the layers.

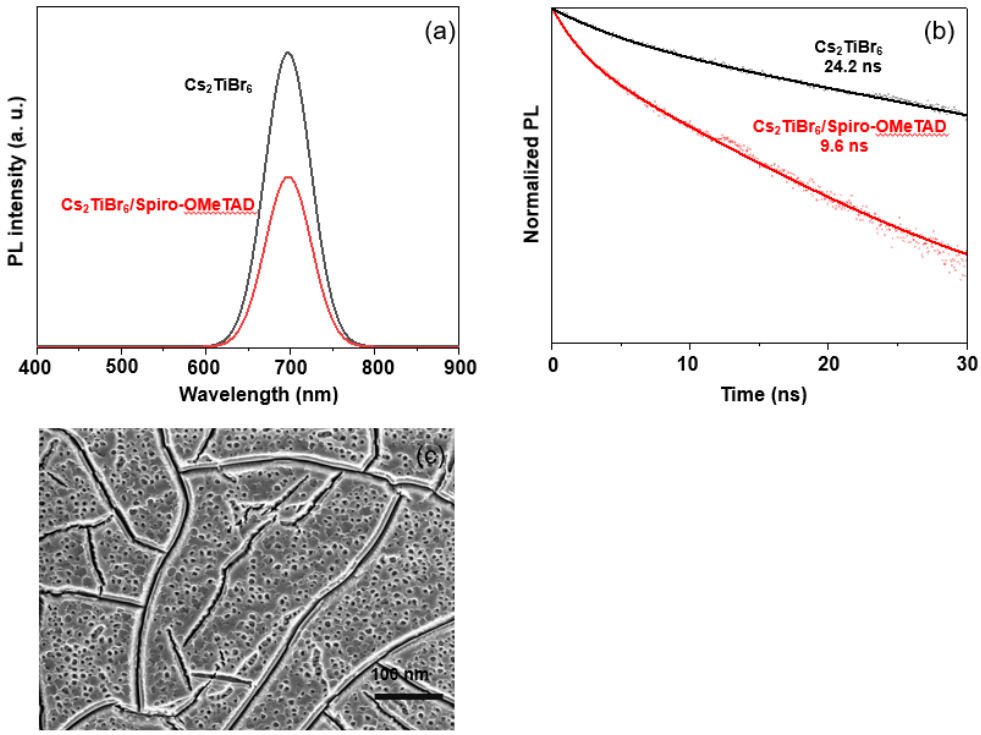

Figure S12. Cs_2TiBr_6 HP thin films were prepared on glass and Spiro-OMeTAD layer was deposited by spin-coating a solution in chlorobenzene (30 mg/ml) at 3000 rpm for 30 s. **(**a) PL spectra from glass/Cs_2TiBr_6 and glass/Cs_2TiBr_6/Spiro-OMeTAD. (b) Time-resolved PL decay of the Cs_2TiBr_6 HP thin film with and without Spiro-OMeTAD hole-quencher. (c) Surface morphology of the samples damaged by the chlorobenzene solvent.

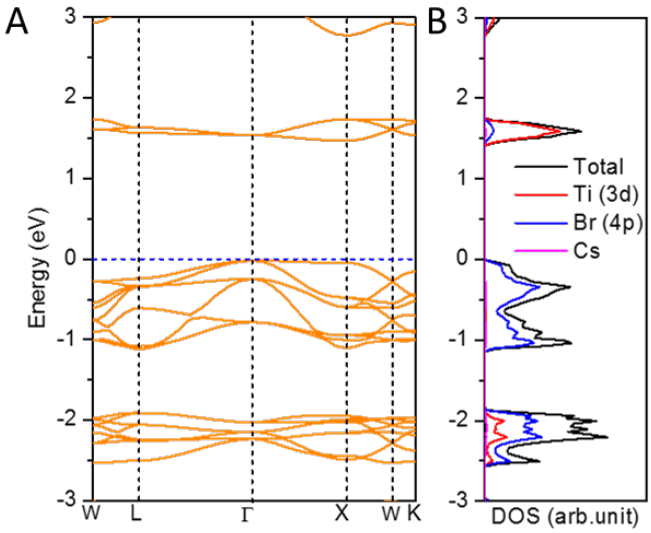

Figure S13. Computed properties of Cs_2TiBr_6 HP using the PBE functional: (A) band structure and (B) DOS and PDOS. Comprehensive understanding of the electronic structure of the Ti-based HP family of materials is presented in our parallel study in Ref. 21 of the main text.

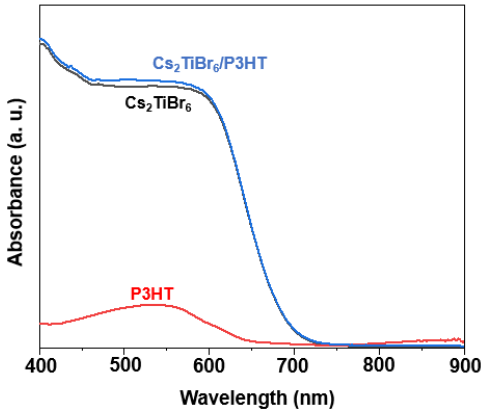

Figure S14. Absorbance spectra for Cs_2TiBr_6, P3HT and Cs_2TiBr_6/P3HT thin films. Cs_2TiBr_6 HP thin films were prepared on a glass substrate, and the P3HT layer was deposited by spin-coating a solution of P3HT in toluene (10 mg/ml) at 3000 rpm, 30 s.

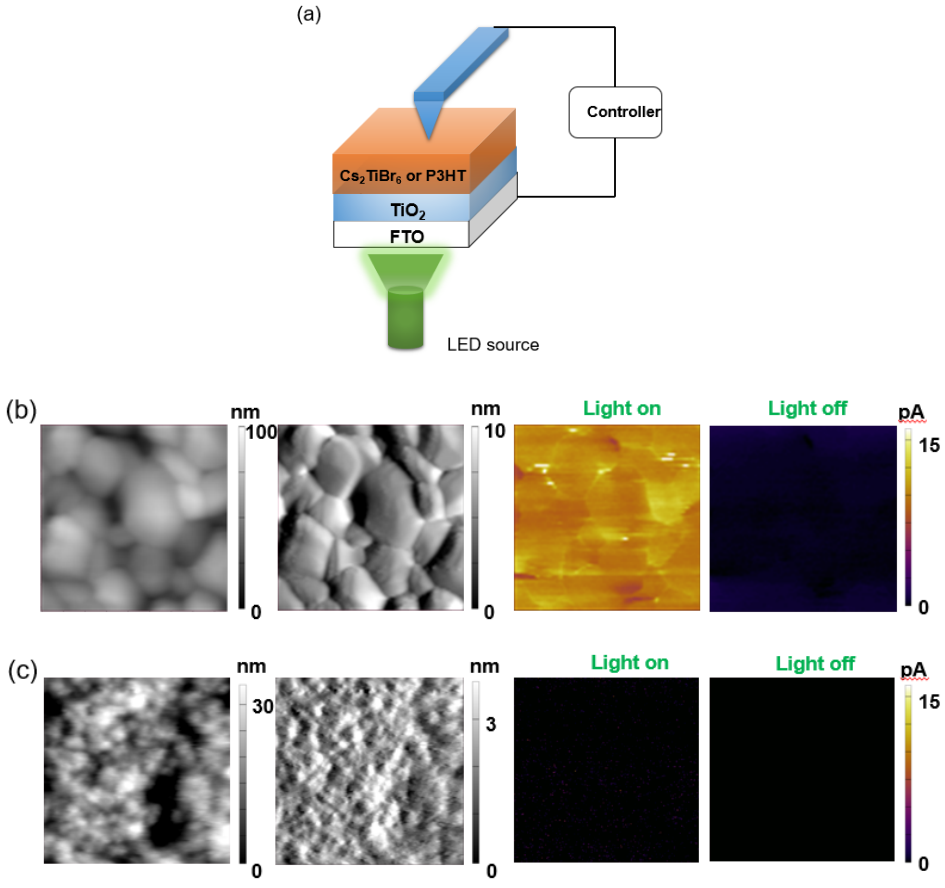

Figure S15. Photoconductive-AFM (*pc*AFM) mapping of Cs_2TiBr_6 HP and P3HT thin films. (a) Schematic illustration of the basic setup for *pc*AFM measurements. The LED source of 567 nm wavelength is used to stimulate photocurrent in the thin film. Topology (left) and photo-response (right) of thin films with light on and light off: (b) Cs_2TiBr_6 HP and (c) P3HT.

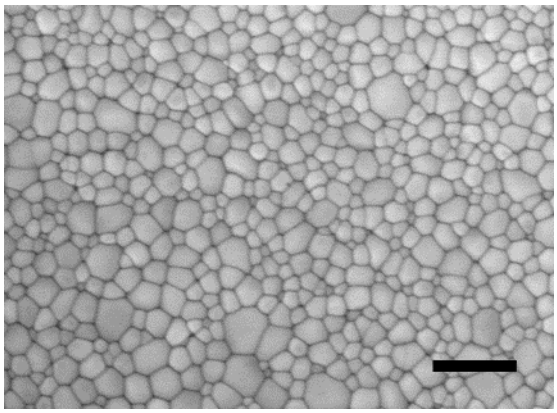

Figure S16. SEM image of top surface of an as-deposited CsBr thin film on a C_{60}-covered substrate. Scale bar = 1 μm.

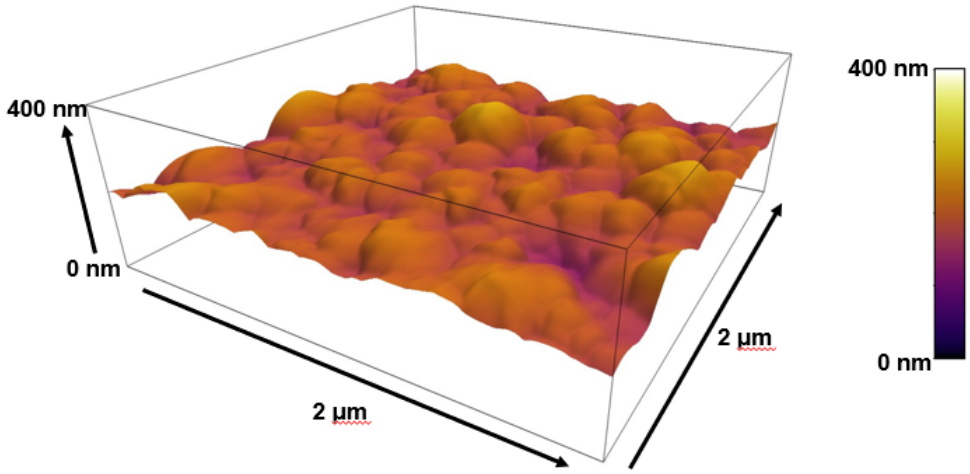

Figure S17. AFM scan of top surface of a Cs_2TiBr_6 HP thin film on C60/TiO_2-coated glass substrate.

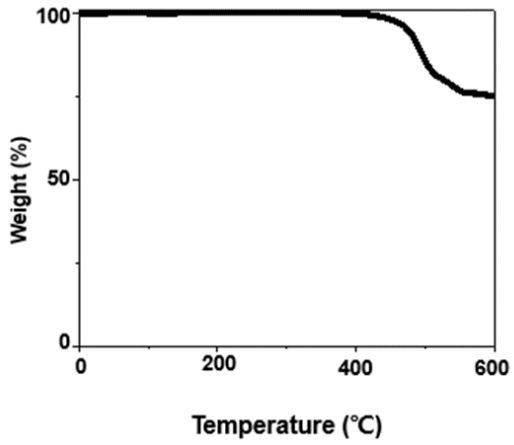

Figure S18. Thermogravimetric analysis (TGA) of Cs_2TiBr_6 HP powder sample.

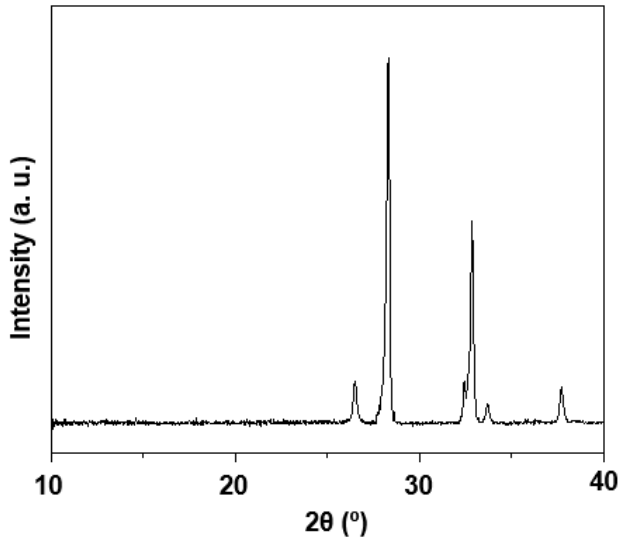

Figure S19. XRD patterns of Cs_2TiBr_6 HP thin film after 24-hour annealing (200 ˚C, N_2 atmosphere).

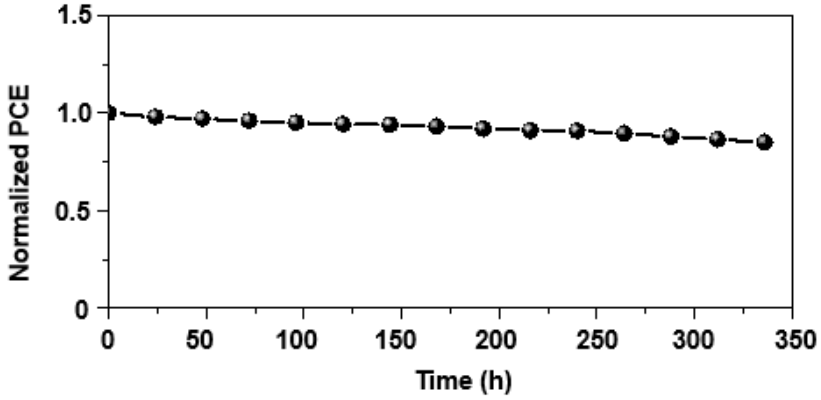

Figure S20. Evolution of PCE of the Cs_2TiBr_6-based PSC (unencapsulated) as a function of the storage time under environmental stress (70 ˚C, 30% RH, one-sun AM 1.5G illumination).